Nanostructures

International Edition: DOI: 10.1002/anie.201603223
German Edition: DOI: 10.1002/ange.201603223

Self-Construction from 2D to 3D: One-Pot Layer-by-Layer Assembly of Graphene Oxide Sheets Held Together by Coordination Polymers

Mohamed B. Zakaria, Cuiling Li, Qingmin Ji, Bo Jiang, Satoshi Tominaka, Yusuke Ide, Jonathan P. Hill, Katsuhiko Ariga, and Yusuke Yamauchi**

Abstract: *Deposition of Ni-based cyanide bridged coordination polymer (NiCNNi) flakes onto the surfaces of graphene oxide (GO) sheets, which allows precise control of the resulting lamellar nanoarchitecture by in situ crystallization, is reported. GO sheets are utilized as nucleation sites that promote the optimized crystal growth of NiCNNi flakes. The NiCNNi-coated GO sheets then self-assemble and are stabilized as ordered lamellar nanomaterials. Regulated thermal treatment under nitrogen results in a Ni_3C–GO composite with a similar morphology to the starting material, and the Ni_3C–GO composite exhibits outstanding electrocatalytic activity and excellent durability for the oxygen reduction reaction.*

For the further development of functional materials, a smart approach to the assembly of functional 2D materials into well-defined 3D structures is critical. The best strategy for this purpose is layer-by-layer (LbL) assembly that can provide well-designed alternating layered structures with nanoscale precision from a variety of functional components.[1] For example, methodologies to create artificial layered structures often lead to materials with high-level functions that cannot be predicted based on the identity of the original components.[2] However, most of the previous strategies have several disadvantages: 1) in many cases, interlayer materials are nonfunctional polymers and often degrade the functionality of the main components; 2) step-by-step layering processes could be disadvantageous for construction of substantially thicker materials. Although pioneering approaches for non-interlayer-polymer LbL processes have been recently proposed,[3] these disadvantages have not yet been properly addressed.

[*] M. B. Zakaria, B. Jiang, Prof. Y. Yamauchi
Faculty of Science and Engineering, Waseda University
3-4-1 Okubo, Shinjuku, Tokyo, 169-8555 (Japan)
E-mail: Yamauchi.Yusuke@nims.go.jp
M. B. Zakaria, Dr. C. Li, Dr. Q. Ji, B. Jiang, Dr. S. Tominaka, Dr. Y. Ide, Dr. J. P. Hill, Prof. K. Ariga, Prof. Y. Yamauchi
World Premier International (WPI) Research Center for Materials Nanoarchitechtonics (MANA)
National Institute for Materials Science (NIMS)
1-1 Namiki, Tsukuba, Ibaraki 305-0044 (Japan)
E-mail: Ariga.Katsuhiko@nims.go.jp
Dr. Q. Ji
Herbert Gleiter Institute of Nanoscience
Nanjing University of Science & Technology
200 Xiaolingwei, Nanjing 210094 (China)
Supporting information and the ORCID identification number(s) for the author(s) of this article can be found under http://dx.doi.org/10.1002/anie.201603223.

In the novel strategy presented here, we have exploited the layering capabilities of coordination polymers[4] as an interlayer adhesive in a spontaneous self-constructive process implemented in one pot. Typically, nickel-based cyano-bridged coordination polymers (NiCNNi) are deposited on the surface of graphene oxide (GO) sheets. During this reaction (Figure 1), GO sheets spontaneously assemble

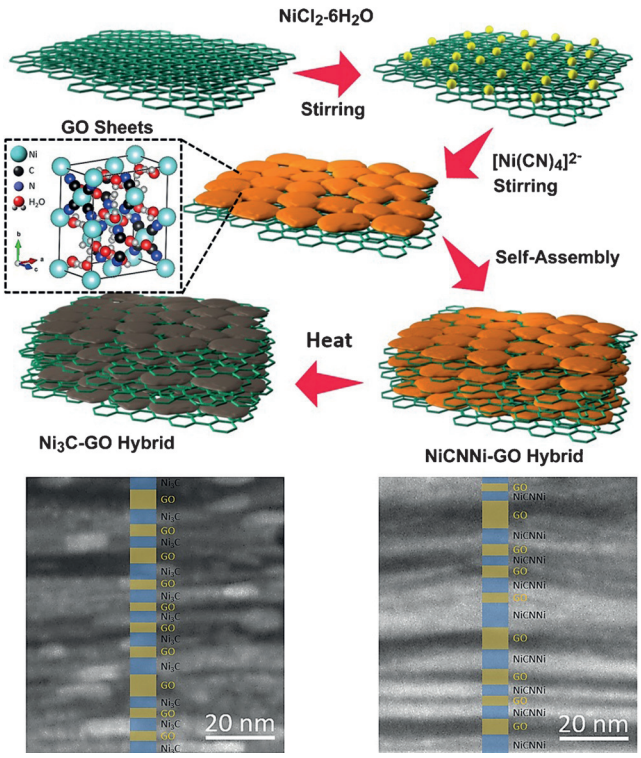

Figure 1. Formation process of NiCNNi–GO hybrids (composites) through layer-by-layer assembly of graphene oxide sheets held together by coordination polymers, and thermal conversion to the Ni_3C–GO hybrid (composite). Cross-sectional TEM images of NiCNNi–GO hybrid and Ni_3C–GO hybrid and the crystal structure of $Ni(H_2O)_2$-$[Ni(CN)_4]$·4 H_2O (NiCNNi) between the GO sheets are also shown.

through binding of NiCNNi flakes in the one-step construction of heterogeneous layered structures whose components all have some potentially useful functionality. In addition, the GO sheets serve not only as building units but also as nucleation sites for the growth of the NiCNNi flakes. Thermal treatment of the layered assembly causes successful conversion of the NiCNNi components to Ni_3C with retention of the original LbL structure, since the inserted GO layers prevent random fusion of the metal source.

Figure 1 shows the formation process of the NiCNNi–GO hybrid structure. The GO sheets have a 2D morphology with a large average lateral dimension of approximately 1 μm and are dispersed as a colloidal suspension (Figure S1). The high-resolution TEM image clearly shows lattice fringes which are oriented in two directions. Electron diffraction (ED) patterns reveal a hexagonal arrangement of the diffraction spots, which is a typical crystalline characteristic of GO. Functional groups (e.g., carboxy, hydroxy, and epoxy)[5] of GO sheets, which can act as bridging sites simultaneously interacting with Ni^{2+} species, confer an overall negative charge onto the starting GO suspension. By slow addition of $[Ni(CN)_4]^{2-}$ into the reaction system, nucleation of growth occurs, resulting in the growth of fine NiCNNi layers on both sides of the GO sheets. During this reaction, the surface charge of GO sheets changes from −30.7 mV to 7.75 mV, according to Zeta potentials measured prior to and following reaction. Subsequently, the NiCNNi–GO components spontaneously assemble forming a highly optimized LbL architecture consisting of alternating layers of NiCNNi and GO.

NiCNNi flakes prepared in the absence of GO sheets exhibit an average lateral size of around 150 nm (Figure S2a,b). The ordered lattice fringes of the flakes from high-resolution TEM (Figure S2c) combined with the periodic spots from the electron diffraction (ED) patterns reveal that the flakes are highly crystallized.[6] The surface morphology of the NiCNNi–GO hybrid was examined using scanning electron microscopy (SEM) and transmission electron microscopy (TEM), and the results are shown in Figure 2. From

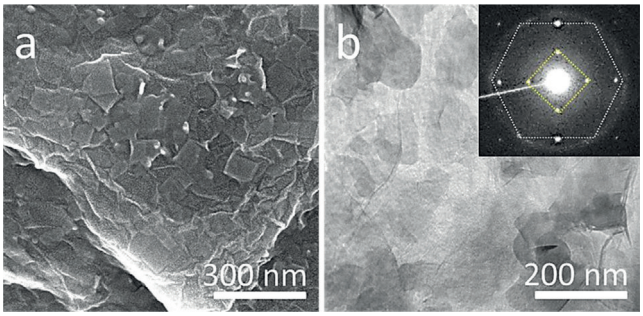

Figure 2. a) SEM image and b) TEM image of the NiCNNi–GO hybrid. Selected-area ED pattern is shown as inset. The spots highlighted by yellow lines are derived from NiCNNi flakes, while those highlighted in white are derived from GO sheets. The respective assignments are given in Figures S1f and S2c.

these images, it can be clearly observed that the NiCNNi flakes have grown horizontally at the surfaces of the GO sheets with flakes apparently encapsulated between the larger GO sheets. The selected-area ED pattern indicates that the crystalline structures of both NiCNNi and GO are preserved even after hybridization (Figure 2b). Interestingly, the cross-sectional high-angle annular dark-field scanning transmission electron microscope (HAADF-STEM) images show an LbL-type structure of the hybrid consisting of NiCNNi and GO layers (Figure 3a and Figure S3a). The corresponding elemental mapping image shows heterogeneous distribution of

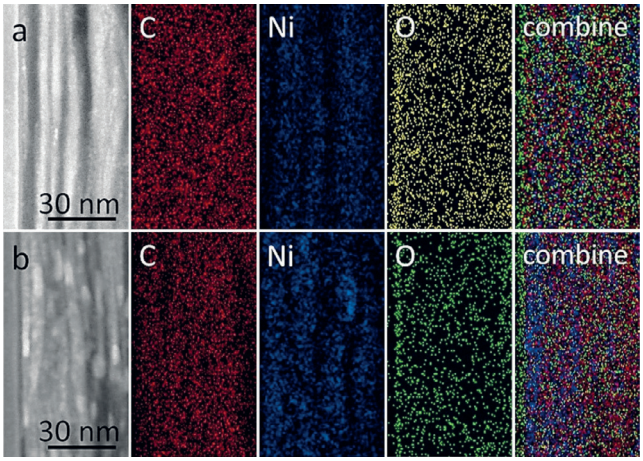

Figure 3. Cross-sectional HAADF-STEM images and elemental mapping images (carbon, oxygen, and nickel atoms) of a) the as-prepared NiCNNi–GO hybrid and b) Ni_3C–GO hybrid after calcination at 450 °C.

Ni, C, and O atoms, thus also supporting the formation of alternating layered structures with nanometer-level layer thicknesses.

To demonstrate the formation process of NiCNNi flakes on the GO sheets, the assembling of layered NiCNNi–GO hybrids was examined by UV/Vis measurements at different time intervals (Figure S4). UV/Vis absorption spectrum of the as-prepared GO suspension shows an absorption peak at around 230 nm corresponding to π–π* transition of C=C and another shoulder at 290–300 nm corresponding to n–π* transition of the C=O bond.[7] As the reaction time is increased from 5 to 90 min, the UV/Vis absorption peaks of NiCNNi–GO hybrids gradually are red-shifted from around 331 nm to 340 nm, corresponding to the d–d transition of Ni. This behavior is evidence of gradual growth of the NiCNNi flakes.[8]

The crystal structures of GO, NiCNNi, and NiCNNi-GO hybrid were further investigated by wide-angle XRD (Figure S5a). In the case of GO, a diffraction peak at 2θ (ca. 9.4°) is observed, corresponding to the 001 reflection (ca. 0.94 nm).[7] Another diffraction peak is observed at 2θ (ca. 25.5°), indicating a highly ordered graphitic structure. The diffraction peaks of the NiCNNi flakes are assignable to an orthorhombic system and clearly match Hofmann-type NiCNNi with 2D layered structure.[6] After the growth of NiCNNi flakes on the GO sheets, the relative peak intensity corresponding to 121 peak is weakened. This observation can be explained by preferential crystal growth on the GO sheets. As shown in Figure 2b, the (121) planes are vertically oriented plane to the GO surface.

The changes of GO structure after the growth of NiCNNi flakes were examined by Raman measurements (Figure S5b). It can be seen that the intensity ratio (I_G/I_D) of the *D* and *G* bands of GO in the NiCNNi–GO hybrid is increased because of the removal of a large number of oxygen-containing functional groups,[7] which means that the GO sheets have less defects. Therefore, as seen in Figure S5a, the 001 peak is weakened and shifted to 2θ (ca. 10.2°), demonstrating a decrease in the distance between two GO sheets (from

ca. 0.94 nm to ca. 0.87 nm). A sharp peak is observed at 2185.7 cm^{-1} that corresponds to C–N stretching,[9] which remains even after hybridization with GO sheets. Together with XPS analysis (Figure S6), we can thus confirm the presence of NiCNNi layers.

It was anticipated that thermal treatment of pristine NiCNNi flakes under nitrogen would result in Ni_3C with a 2D morphology. To test this hypothesis, NiCNNi flakes without GO sheets were calcined under nitrogen at different temperatures (i.e., 350 °C, 450 °C, 550 °C, and 650 °C, respectively). The crystal structures and phase purities of the resulting products were examined by using wide-angle XRD (Figure S7). The sample calcined at 350 °C underwent incomplete removal of the organic units and the peaks could not be assigned to a specific crystal structure. Interestingly, the sample calcined at 450 °C gives a diffraction pattern characteristic of pure crystalline Ni_3C with XRD patterns assignable to a trigonal ($R\bar{3}c$) structure.[10] Further increases in the calcination temperature (500 °C and 650 °C) led to decomposition of the Ni_3C structure with some peaks corresponding to metallic face-centered cubic Ni emerging. Although pure crystalline Ni_3C could be obtained following optimization of the thermal treatment process of NiCNNi flakes (i.e., 450 °C under nitrogen), the original 2D form was totally disrupted because of crystallization and fusion of the metal framework, as illustrated by SEM imaging (Figure S8). In contrast, the NiCNNi–GO LbL structure is relatively stable, even against thermal treatment at elevated temperatures, which results in the Ni_3C–GO LbL structure. The Ni_3C–GO hybrid has an LbL structure that strongly corresponds with the original NiCNNi–GO hybrid (Figure 3b, Figure S3b). As is clearly shown in Figures S9 and S10, the lateral size and morphology of individual Ni_3C nanosheets remains unchanged.

The Ni_3C–GO hybrid obtained by calcination at 450 °C was examined by high resolution X-ray photoelectron spectroscopy (XPS; Figure 4a–c). At least seven peaks are found in the C 1s XPS spectrum after deconvolution. The peak at 283.3 eV is assigned to Ni–C bonds,[11] with a second peak at 285.5 eV assigned sp^3-hybridized carbon atoms in C–C bonds.[11] Between these two peaks, a third feature at 284.3 eV can be assigned to sp^2 hybridized carbon atoms in C=C bonds.[11] Additionally, four types of carbon atoms in different functional groups can be observed: non-oxygenated ring (284.5 eV), C–O (286.01 eV), C=O (288.42 eV), and O–C=O (292 eV).[12] In the Ni $2p_{3/2}$ XPS spectrum, a peak with a binding energy of 855.4 eV with a satellite peak at 861.6 eV were observed. The main peak position is located at a higher binding energy than NiO, $Ni(OH)_2$, and metallic Ni phases, and it corresponds to pure Ni_3C phase. From these XPS data, it can be deduced that the Ni_3C flakes are more tightly anchored to the surface of GO through oxygen-containing functional groups. Raman spectra of GO sheets and Ni_3C–GO hybrids are shown in Figure 4d. The *D* and *G* bands of GO sheets can be clearly observed in both cases,[13] thus implying the retention of 2D GO structure even after the growth of Ni_3C during thermal treatment. After heat treatment, the intensity of the graphitic (*G*) band increases relative to that of GO sheets because the functional groups of GO sheets have been thermally decomposed.

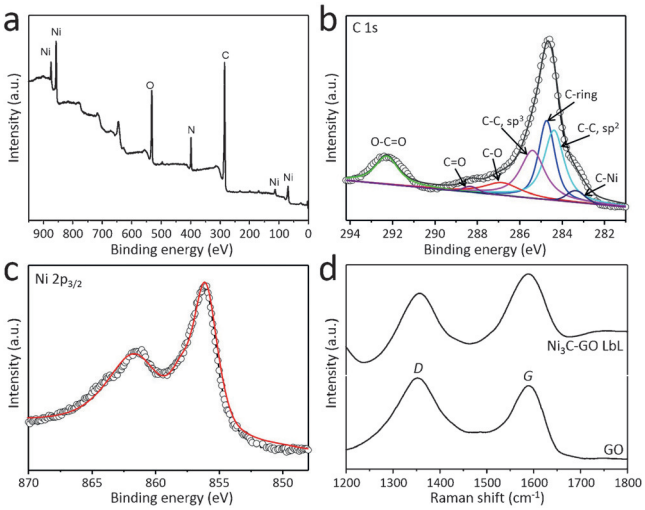

Figure 4. a) XPS survey spectrum and XPS expanded spectra b) C1s and c) Ni $2p_{3/2}$ of Ni_3C–GO hybrid after calcination at 450 °C. d) Raman spectra of GO sheets and Ni_3C–GO hybrid after calcination at 450 °C.

Of the well-known transition metal carbides, nickel carbide (Ni_3C) has received considerable recent attention owing to its excellent catalytic activity and high chemical stability.[14] It is anticipated that Ni might be a realistic alternative to precious metals such as Pt, Au, and Pd, because of its low cost, abundance, and corrosion resistance in alkaline solutions.[14] However, Ni_3C has been much less investigated because complex synthetic procedures, which require expensive apparatus. A few previous reports have suggested that thermal treatment of nickel-based precursors might allow the synthesis of high-quality Ni_3C,[15] although morphological control and particle aggregation at elevated temperatures remain challenging issues. The integration of transition-metal carbides and highly conductive carbon materials could also circumvent serious problems associated with the rate capabilities and poor charge transport. The intrinsic properties of graphene (e.g., excellent electrical conductivity and high mechanical strength) would make its hybrids with Ni_3C excellent candidates for various electronic applications. In this work, we demonstrate the significant advantage of an LbL architecture for such materials over simple physically mixed Ni_3C–GO composites.

Inspired by the unique form of the LbL-structured Ni_3C–GO hybrid after calcination at 450 °C (abbreviated as Ni_3C–GO LbL), the oxygen reduction reaction (ORR) was investigated to explore the potential application of these materials in energy-conversion systems. Its electrocatalytic activity was also benchmarked against GO, Ni_3C, and a physically mixed Ni_3C–GO composite (abbreviated as Ni_3C–GO mix). The electrocatalytic activities of all the samples were first evaluated by cyclic voltammetry (CV) in 0.1 M KOH solution saturated with N_2 and O_2 at a scan rate of 20 mV s^{-1}. The observed oxygen-reduction peak of Ni_3C–GO LbL shifted significantly to more positive potentials (−290 mV vs. Ag/AgCl) than that of GO (−310 mV vs. Ag/AgCl), Ni_3C (−370 mV vs. Ag/AgCl), or Ni_3C–GO mix (−360 mV vs. Ag/AgCl), as shown in Figure S11, thus suggesting the

significantly enhanced electrocatalytic activity of the LbL-structured Ni_3C–GO hybrid.

The performance of the samples in the ORR was further examined by using a rotating ring-disk electrode (RDE) in an O_2-saturated 0.1 M KOH solution at a rotation speed of 1600 rpm and a scan rate of 10 mV s^{-1} (Figure 5). The linear-

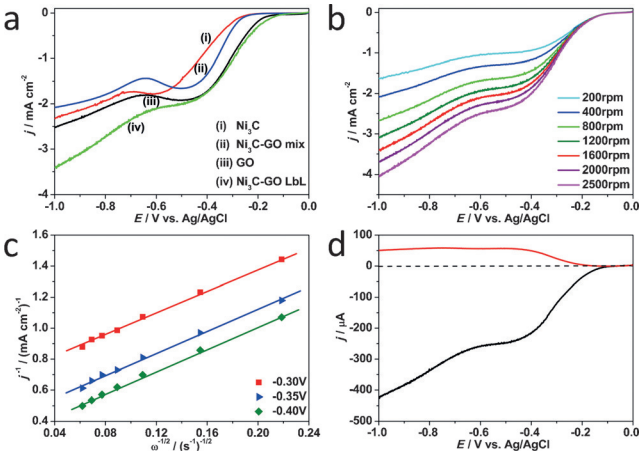

Figure 5. a) ORR polarization curves of i) Ni_3C, ii) Ni_3C–GO mix, iii) GO, and iv) Ni_3C–GO LbL, recorded in O_2-saturated 0.1 M KOH solution with a sweep rate of 10 mV s^{-1} at a rotation rate of 1600 rpm. b) ORR polarization curves of Ni_3C-GO LbL at different rotation rates. c) Corresponding Koutecky–Levich (K–L) plots of the Ni_3C–GO LbL at different potentials. d) Current collected on disk and ring electrodes catalyzed by Ni_3C–GO LbL.

sweep hydrodynamic voltammograms (LSV) in Figure 5a confirm the ORR activity of Ni_3C–GO LbL catalyst, with an onset potential of around −99 mV vs. Ag/AgCl. Compared to GO (−166 mV vs. Ag/AgCl), Ni_3C (−240 mV vs. Ag/AgCl), and Ni_3C–GO mix (−228 mV vs. Ag/AgCl), the Ni_3C–GO LbL (−99 mV vs. Ag/AgCl) shows a more positive onset potential, thus further confirming the improved electrocatalytic activity of the Ni_3C–GO LbL catalyst for the ORR. Even when compared to previous reports, our Ni_3C–GO LbL catalyst shows a more positive onset potential, as summarized in Table S1.

To investigate the effect of the Ni_3C–GO LbL catalyst on the kinetics of the ORR, the RRDE measurement was performed at different rotation speeds from 200 rpm to 2500 rpm at a constant scan rate of 10 mV s^{-1} (Figure 5b). The corresponding Koutecky–Levich plots[16] (j^{-1} vs. $\omega^{-1/2}$) for our catalysts are parallel with good linearity and constant electron transfer numbers for ORR at different potentials (−0.30, −0.35, and −0.40 V vs. Ag/AgCl), as shown in Figure 5c. The average number of transferred electrons (n) was estimated to be 2.6 which is slightly higher than that of 2.5 for the Ni_3C–GO mix (Figure S12).

Moreover, to obtain a more in-depth understanding of the ORR process, the number of transferred electrons (n) was estimated from hydrodynamic voltammograms collected from the disk and ring electrodes. The obtained n values during the ORR using the Ni_3C–GO LbL catalyst was estimated to be from 2.6 to 3.0 (from −0.4 V to −1.0 V vs. Ag/AgCl) (Figure 5d). Furthermore, the charge-transfer resistances of the Ni_3C–GO LbL and Ni_3C–GO mix catalysts were investigated by electrochemical impedance spectroscopy (EIS) in 0.1 M KOH over the frequency range from 1 MHz to 1 Hz. The typical impedance spectra of different catalysts are shown in Figure S13. The diameters of the semicircle behaviors of the EIS data represent the charge-transfer resistance (R_{ct}) at the electrode surface. It is obvious that the layer-by-layer assembled Ni_3C–GO sample shows lower resistance, namely better performance, than the physically mixed sample (Ni_3C–GO mix).

In conclusion, we have synthesized NiCNNi–GO LbL hybrids through the layer-by-layer assembly of graphene oxide sheets held together by coordination polymers, in which the GO sheets serve not only as building units but also as nucleation sites for the growth of NiCNNi flakes. Even after thermal treatment, the layered NiCNNi parts are successfully converted to Ni_3C with retention of the original LbL structure because the inserted GO layers effectively prevent random fusion of the metal source. Our method relies on the layering capabilities of coordination polymers and their interlayer adhesive properties for spontaneous LbL construction. Our approach should also be applicable to the synthesis of many other inorganic–organic hybrids with ordered LbL architectures. Thus, a variety of well-designed alternating layered nanoscale structures with novel properties will be realized by varying the initial functional components in our synthetic scheme.

Keywords: coordination polymers · hybrid materials · lamellar structures · layer-by-layer structures · metal carbides

How to cite: *Angew. Chem. Int. Ed.* **2016**, *55*, 8426–8430
Angew. Chem. **2016**, *128*, 8566–8570

[1] a) K. Ariga, Y. Yamauchi, G. Rydzek, Q. Ji, Y. Yonamine, K. C.-W. Wu, J. P. Hill, *Chem. Lett.* **2014**, *43*, 36–68; b) J. Borges, J. F. Mano, *Chem. Rev.* **2014**, *114*, 8883–8942; c) J. J. Richardson, M. Björnmalm, F. Caruso, *Science* **2015**, *348*, 411; d) R. F. Fakhrullin, Y. M. Lvov, *ACS Nano* **2012**, *6*, 4557–4564; e) T. G. Shutava, P. P. Pattekari, K. A. Arapov, V. P. Torchilin, Y. M. Lvov, *Soft Matter* **2012**, *8*, 9418–9427; f) Y. Jia, J. Li, *Chem. Rev.* **2015**, *115*, 1597–1621; g) P. Cai, X. Feng, J. Fei, G. Li, J. Li, J. Huang, J. Li, *Nanoscale* **2015**, *7*, 10908–10911.

[2] a) M. Osada, T. Sasaki, *Adv. Mater.* **2012**, *24*, 210–228; b) R. Ma, T. Sasaki, *Acc. Chem. Res.* **2015**, *48*, 136–143.

[3] a) H. Wang, S. Ishihara, K. Ariga, Y. Yamauchi, *J. Am. Chem. Soc.* **2012**, *134*, 10819–10821; b) R. Ma, X. Liu, J. Liang, Y. Bando, T. Sasaki, *Adv. Mater.* **2014**, *26*, 4173–4178.

[4] a) R. Makiura, S. Motoyama, Y. Umemura, H. Yamanaka, O. Sakata, H. Kitagawa, *Nat. Mater.* **2010**, *9*, 565–571; b) S. Motoyama, R. Makiura, O. Sakata, H. Kitagawa, *J. Am. Chem. Soc.* **2011**, *133*, 5640–5643.

[5] S. Eigler, A. Hirsch, *Angew. Chem. Int. Ed.* **2014**, *53*, 7720–7738; *Angew. Chem.* **2014**, *126*, 7852–7872.

[6] M. B. Zakaria, M. Hu, R. R. Salunkhe, M. Pramanik, K. Takai, V. Malgras, S. Choi, S. X. Dou, J. H. Kim, M. Imura, S. Ishihara, Y. Yamauchi, *Chem. Eur. J.* **2015**, *21*, 3605–3612.

[7] Z. Luo, Y. Lu, L. A. Somers, A. T. C. Johnson, *J. Am. Chem. Soc.* **2009**, *131*, 898–899.

[8] L. Espinosa-Alonso, K. P. de Jong, B. M. Weckhuysen, *J. Phys. Chem. C* **2008**, *112*, 7201–7209.

[9] a) M. A. Omary, T. R. Webb, Z. Assefa, G. E. Shankle, H. H. Patterson, *Inorg. Chem.* **1998**, *37*, 1380 – 1386; b) E. Hesse, J. A. Creighton, *Chem. Phys. Lett.* **1999**, *303*, 101 – 106.
[10] W. Zhou, K. Zheng, L. He, R. Wang, L. Guo, C. Chen, X. Han, Z. Zhang, *Nano Lett.* **2008**, *8*, 1147 – 1152.
[11] A. Furlan, J. Lu, L. Hultman, U. Jansson, M. Magnuson, *J. Phys. Condens. Matter* **2014**, *26*, 415501.
[12] a) D. R. Dreyer, S. Park, C. W. Bielawski, R. S. Ruoff, *Chem. Soc. Rev.* **2010**, *39*, 228 – 240; b) S. Pei, H.-M. Cheng, *Carbon* **2012**, *50*, 3210 – 3228.
[13] a) P. Sun, M. Zhu, K. Wang, M. Zhong, J. Wei, D. Wu, H. Zhu, *ACS Appl. Mater. Interfaces* **2013**, *5*, 9563 – 9571; b) Z.-S. Wu, W. Ren, L. Gao, J. Zhao, Z. Chen, B. Liu, D. Tang, B. Yu, C. Jiang, H.-M. Cheng, *ACS Nano* **2009**, *3*, 411 – 417.
[14] a) M. Jiao, K. Li, W. Guan, Y. Wang, Z. Wu, A. Page, K. Morokuma, *Sci. Rep.* **2015**, *5*, 12091; b) Z. Zhou, J. Wang, W. Liu, C. Yu, B. Kong, Y. Sun, H. Yang, S. Yang, W. Wang, *Nanoscale* **2014**, *6*, 12591 – 12600.
[15] a) Y. Goto, K. Taniguchi, T. Omata, S. Otsuka-Yao-Matsuo, N. Ohashi, S. Ueda, H. Yoshikawa, Y. Yamashita, H. Oohashi, K. Kobayashi, *Chem. Mater.* **2008**, *20*, 4156 – 4160; b) Z. L. Schaefer, K. M. Weeber, R. Misra, P. Schiffer, R. E. Schaak, *Chem. Mater.* **2011**, *23*, 2475 – 2480.
[16] J. Tang, J. Liu, C. Li, Y. Li, M. O. Tade, S. Dai, Y. Yamauchi, *Angew. Chem. Int. Ed.* **2015**, *54*, 588 – 593; *Angew. Chem.* **2015**, *127*, 598 – 603.

Received: April 1, 2016
Published online: May 11, 2016

